Experimental investigations on acoustic-velocity-flame dynamic characteristics of a stratified burner

*Ming JIN [a], Yudi LU [a], Yuansen LI [a], Weijie LIU [b], Bing GE[a] *, Shusheng ZANG [a]*

a. *School of Mechanical Engineering, Shanghai Jiao Tong University, Shanghai 200240, China;*
b. *Zhejiang University, Hangzhou 310058, China*
email: gebing2017@163.com

Abstract: *To reveal the influence of interaction between pilot and main flames on flow and thermo-acoustic instability characteristics, high-frequency measurement devices such as High-Frequency Particle Image Velocimetry (HFPIV), high-speed camera, pressure sensors, and photomultiplier tube were applied to study the acoustic-velocity-flame dynamic characteristics of the stratified burner under ambient temperature and pressure. Results show that the pilot swirling flow significantly influences the acoustic-velocity-flame dynamic characteristics of the stratified burner. When the pilot and main stage are operated with a swirling air jet and swirling flame, the main recirculation zone disappears, the thermo-acoustic instability is strengthened and the frequency of thermo-acoustic instability is locked with the large-scale vortex shedding frequency. When the pilot stage is converted into a swirling flame, the main recirculation zone re-appears downstream of the nozzle outlet, and the high-temperature burned gas is rolled back to improve the combustion stability of the swirling flame. However, in this case, the interaction between the pilot and main flames makes the thermo-acoustic instability frequency not well consistent with large-scale vortex shedding frequency. the interaction between the main stage and pilot stage flames leads to the increase of the flame angle of the main stage. The heat release fluctuation at the flame interaction region is the most intense, and the large-scale vortex in the outer shear layer of the main stage also causes the flame to produce severe oscillation.*

Keywords: *stratified burner, flame interaction, flow interaction, thermo-acoustic instability, flow instability*

1. Introduction

To reduce NOx emission, the lean premixed combustor is widely used in aero-engine and ground gas turbines, and combustion instability is one of the main challenges of the lean premixed combustor. The external manifestation of combustion instability is the periodic high amplitude pressure pulsation caused by the coupling of the system sound field and unsteady heat release, which will lead to flame flashback and blowoff, and may even lead to structural damage of the system. To broaden the range of stable combustion conditions, some low-emission combustor is designed as stratified structure, that is, the combustor includes the

precombustion stage and main combustion stage. The main combustion flame is stabilized by the oil-rich precombustion stage flame, which can reduce emission [1,2].

The shear layer of the rotating jet usually produces periodic vortices, which has an important effect on the dynamic characteristics of the flame [3-5]. Wang [6] applied PIV to study the effect of the flow field on the local flame fronts and found that the flame paths of motion are greatly influenced by the flow structure of the annular combustor. Menon [7] obtained the sound equation and vortex equation of the combustion state by theoretical derivation. The interaction between flame and vortex is an important mechanism of flame nonlinear response [8-10]. Bellows [11] observed the nonlinearity of vortex flame in an industrial gas turbine. They found that the nonlinearity of flame response is related to vortex rolling. Kumar [12] found that flame dynamic is controlled by four processes: annular jet wave, pulsating turbulent flame brush development, the flame and flow instability pulsation. Schimek [13,14] found that the pulsation of flame is caused by the interaction between the vortex and flame. Terhaar [15] and Oberleithner [16] found that shear flow instability is an important driving factor of flame pulsation. Palies [17,18] concluded that the dynamic response of the unstable heat release rate is determined by the combined influence of the axial and induced azimuth velocity perturbations, which also cause the swirl number pulsation. Terhaar [19] studied the excitation of the precession vortex core and the suppression of flame pulsation by sound velocity perturbation experimentally and theoretically.

The coupling effect between vortex and flame is mainly studied on a single swirling flame. Compared with a single swirling flame, a centrally staged combustor has a more complex structure. The flame structure and dynamic characteristics are also more complex and varied. Ma [20] Studied the Influence of the co- and counter-swirl on the combustion instability of the centrally staged combustor. Results depicted that the heat release regions of the counter-swirl scheme are mainly concentrated in the shear layer and the counter-swirl scheme exhibits larger vorticities and strain rates in the ISL (ISL, Inner Shear Layer) and OSL (OSL, Outer Shear Layer). Chong [21] found that the increase in precombustion stage mass flow will form a longer flame and stronger reaction zone. Kim [22] found that the distribution of the equivalent ratio of the precombustion stage and main combustion stage determines the flame form and dynamic characteristics. Han [23] studied the mechanism of the precombustion stage flame of a simplified central stage burner on the stable main combustion stage flame by experiment. Lv [24] investigated the effects of the pilot-stage equivalence ratio on combustion instabilities in a coaxial staged model combustor and found that the pilot-stage equivalence ratio influenced the heat release rate and flame transfer function significantly. Previous studies mainly analyzed the influence of the precombustion stage and main combustion stage flame interaction on the dynamic characteristics of the central stage burner. However, for the precombustion stage and the main stage flame independently, as there is no interaction between flames, the difference in the flow-thermal-acoustic dynamic characteristics compared with the stratified flame requires further study.

In this paper, the flow and thermo-acoustic dynamic characteristics of the pilot stage, main stage, and stratified flame in the combustion chamber of the stratified model combustor are studied by experiments and calculations. By means of high-frequency PIV, high-speed camera, photomultiplier tube, and pulsating pressure sensors, the unsteady flow field, flame

CH* signal distribution, global heat release rate, and pressure pulsation characteristics under different testing conditions were measured respectively. Combined with simplified acoustic mode calculation of the combustor, the influences of the interaction between the pilot flame and main flame on the combustor acoustic mode were obtained. The unsteady flow and thermo-acoustic instability of single stage swirling flame and stratified flame in the stratified burner were revealed.

2. Experimental setup and diagnostic
2.1 Experimental setup

The acoustic-velocity-flame dynamic characteristics experimental system of the stratified burner is shown in Fig. 1. It consists of an air and fuel system, inlet section, acoustic driving unit, stratified burner, optical combustion chamber, and exhaust section. The inlet section is 270 mm long and the inner diameter is 43.5 mm. Two microphones P_A and P_B are set on the inlet tube with an axial distance of 60 mm. The stratified burner is installed at the end of the inlet section. The air is supplied at room temperature and pressure, and the fuel is fed with high-purity methane. The volume flowmeters are used to measure the air and fuel flow rate. Before entering the combustion chamber, fuel and air are well-premixed in the stratified burner. Two quartz windows are opened on the sidewalls of the combustor, providing optical access to the flame and flow field. The cross-section of the optical combustor is square and the size is 140×140 mm. After burning in the combustor, the burned gas is exhausted into the atmosphere.
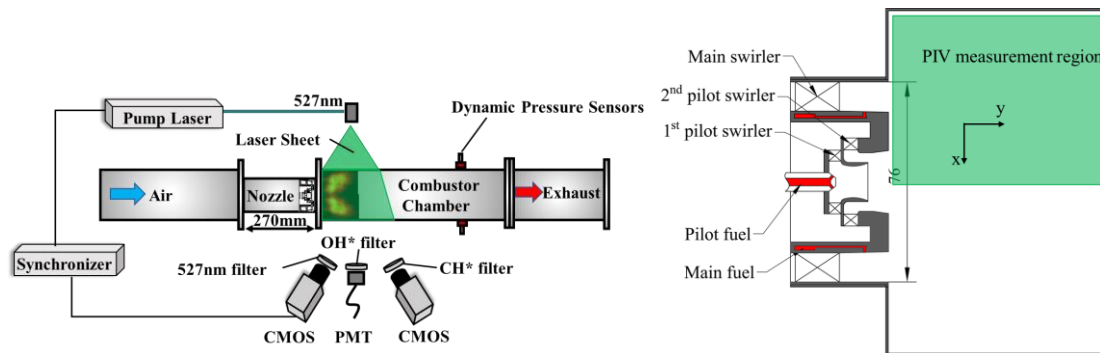
Figure 1. Sketch of experimental setup and stratified burner.

The detailed structure of the stratified burner is shown in Fig. 1. The multi-burner has a pilot stage and a main stage. The pilot stage is arranged in the center of the burner with a typical swirler cup design which includes dual counter-rotating radial swirlers. The main stage surrounding the pilot stage consists of an axial swirler fitted with sixteen constant-thickness vanes. The diameter of the main stage is $d_0=76$ mm. The swirling direction of the main stage is the same as the secondary pilot stage. According to the definition of the geometric swirl number [25], the swirl numbers of the primary, secondary pilot stage, and main stage are 0.73, 0.58, and 0.73, respectively.

The flow field is measured using high-frequency Particle Imaging Velocimetry (HFPIV). The HFPIV system is mainly composed of a double pulsed Nd: YAG laser (Beamtech) and a

high-speed Complementary Metal Oxide Semiconductor (CMOS) camera (VEO 710L) with 1280×800 pixels resolution. The laser produces dual pulsed laser beams with 31.5 mJ/pulse @ 527 nm at a repetition rate of 1000 Hz. The laser beam is expanded by a set of spherical and cylindrical lenses, forming a laser sheet with a thickness of about 1 mm. The laser sheet is guided vertically through the center plane in the combustion chamber as shown in Figure 1. The high-speed CMOS camera is equipped with a 60 mm F/2.8 Nikkor lens and a narrow-band filter of wavelength 527±10 nm, and it is synchronized with the laser at a frame rate of capturing image pairs of 1000 Hz. TiO_2 particles with a nominal diameter of 2 μm are added to the airflow before the inlet section using a seeding generator. The raw image pairs are saved and processing is carried out with an adaptive cross-correlation program (Dynamic Studio 6.3 by DANTEC). The image pairs are divided into squared interrogation areas whose final dimensions are 16×16 pixels with an overlap of 50%.

A narrow-band filter with a wavelength of 432 nm±10 nm is installed in front of the high-speed camera lens (Nikkor 70-200 mm f / 2.8) to capture the transient change of the CH* signal distribution. The image resolution is 1280 × 800 pixels, the sampling rate is 1000 Hz, and the acquisition duration is 0.5 seconds.

The photomultiplier tube (PMT, Hamamatsu H10723-210) is installed with a 307 nm±10 nm narrow-band filter to measure the global flame OH* emission intensity and characterize the global flame heat release rate. The dynamic pressure of the combustion chamber is collected by the Kulite pressure sensors installed on the wall of the combustion chamber. The dynamic pressure and global flame heat release rate are recorded synchronously at a sampling frequency of 20000 Hz by the National Instruments data acquisition system.

2.2 Data Processing Method

The experiment is carried out under four conditions. (1) P_aM_a (pilot air + main air), (2) P_fM_a (pilot flame + main air), (3) P_aM_f (pilot air + main flame), (4) P_fM_f (pilot flame+ main flame). In the test, the inlet bulk velocity of the burner is U_0 = 10.1 m / s, and the air distribution ratio between the pilot stage and the main stage is 7:43, and the detailed test conditions are shown in Table 1.

Table 1. Test conditions.

case	Operating Mode	Φ_p	Φ_m	Φ_{total}	Power (kW)
P_aM_a	pilot air + main air	0	0	0	0
P_fM_a	pilot flame + main air	1.3	0	0.14	7.1
P_aM_f	pilot air + main flame	0	0.6	0.54	27.6
P_fM_f	pilot flame + main flame	1.3	0.6	0.67	34.7

In this paper, the acoustic-velocity-flame dynamic characteristics of the stratified burner under different testing conditions are studied experimentally. The frequency spectrum characteristics of thermo-acoustic instability under different conditions are obtained by the

Fast Fourier Transform (FFT) based on global flame OH* emission intensity and combustor dynamic pressure signals. Swirling flames usually induce large-scale coherent structures in the swirling flow shear layer, such as shedding vortices. The proper orthogonal decomposition (POD) method can be used to analyze the unsteady flow field and study the dynamic characteristics of shedding vortices in the flow field [26].

The Proper Orthogonal Decomposition (POD) was first introduced in the context of Fluid Mechanics by Lumley [27]. POD is a powerful method to capture the dominant flow features and extract the coherent structures from the flow field. With the benefit that a small number of POD modes can represent the dynamic evolution of the turbulent flow, it has been applied in several previous investigations. This implementation of POD in the present study applies the so-called "Snapshot POD" proposed by Sirovich [28]. The first step is to calculate the mean velocity field from all the snapshots. The mean velocity field is considered as the zero'th mode of the POD. Subtracting the mean velocity part from all the instantaneous flow fields, the fluctuating parts of the velocity components from the N snapshots can be given as:

$$u'_{mt} = u_{mt} - \frac{1}{N}\sum_{t=1}^{N} u_{mt} \tag{1}$$

Where u' and u denote fluctuating and instantaneous velocity of each snapshot, index m and t run through the M positions of velocity vectors and the N snapshots, respectively. All fluctuating velocity components from all snapshots can be arranged in a matrix U. Then the auto-covariance matrix C and the corresponding eigenvalue λ_i and eigenvector $\emptyset_i$ can be solved as:

$$C = U^T U \tag{2}$$

$$C\phi_i = \lambda_i \phi_i \tag{3}$$

Finally, the POD mode φ_i could be computed as:

$$\varphi_i = \frac{U\phi_i}{\|U\phi_i\|} \tag{4}$$

The POD coefficient a can be simulated by:

$$a = \psi^T U \tag{5}$$

Where each of the POD modes φ_i occupy the mode matrix Ψ.

Since the POD time coefficient value represents the contribution rate of a certain mode to each instantaneous velocity field, the contribution rate of the mode to the continuous flow field can be obtained. The FFT of the POD time coefficient value of the selected mode can be used to obtain the periodic frequency of the corresponding coherent structure.
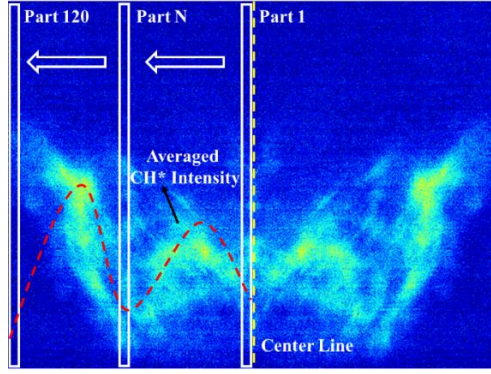
Figure 2. Partition diagram of flame CH * intensity distribution.

The CH* emission intensity contour is divided into several parts along the radial direction, and the CH* intensity in each part is integrated to obtain the area-weighted average CH* intensity. As shown in Fig. 2, the CH* distribution is divided into 120 parts on the left side of the central axis of the burner, that is, every 5 pixels along the radial direction is divided into 1 part. The area-weighted average CH* intensity $I_{t\,CH*}$ in the part of each transient moment is calculated by equation (6). Based on the 500 successive CH* emission intensity contours, the Root mean square (RMS) CH* intensity in each part is obtained by the RMS calculation formula, which is used to characterize the flame oscillation intensity at different positions along the radial direction.
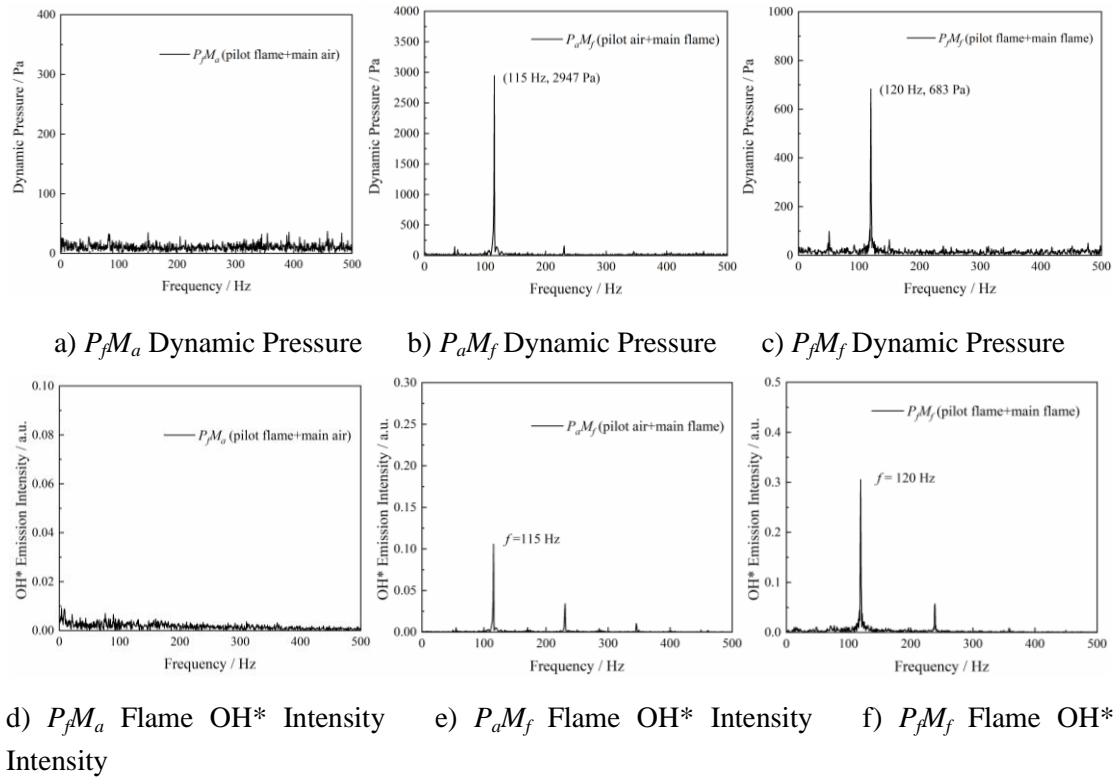
$$\bar{I}_{tCH*} = \frac{1}{A_i} \iint_{Part_i} I_{tCH*} dx dy \quad . \tag{6}$$

In equation (6), the area-weighted average CH* intensity of the i-th part at time t is represented as $I_{t\,CH*}$. *Part i* is the *i*-th part, *Ai* is the area of the *i*-th part, and the CH* intensity of each pixel in the *i*-th part at time *t* is represented as I_{tCH*}.

3 Results and Discussions

3.1 Thermo-acoustic Instability

Fig. 3 shows the spectrums of dynamic pressure and global flame OH* detected with PMT. For the P_fM_a operating condition, the pressure and OH* spectrums do not present any dominant frequency, and the amplitude of pressure is approximately 50 Pa, which indicates the P_fM_a operating condition is pretty stable. For the P_aM_f operating condition, the pressure and OH* spectrums show the same dominant frequency of 115 Hz, and the amplitude of pressure is about 2947 Pa. When the amplitude of pressure exceeds 0.5% of the mean combustor pressure, combustion is thought to be unstable [29,30], which means P_aM_f operating condition is suffering strong thermo-acoustic instability. For the P_fM_f operating condition, the pressure and OH* spectrums also show the same dominant frequency of 120 Hz, which is slightly shifted compared with the P_aM_f operating condition. However, the pressure oscillation has been largely suppressed and its amplitude is about 693 Pa. This reveals the interaction between the pilot and main flames results in the difference in combustion instability frequency and pressure oscillation amplitude between P_aM_f and P_fM_f operating conditions.

a) P_fM_a Dynamic Pressure   b) P_aM_f Dynamic Pressure   c) P_fM_f Dynamic Pressure

d) P_fM_a Flame OH* Intensity   e) P_aM_f Flame OH* Intensity   f) P_fM_f Flame OH* Intensity

Figure 3. Dynamic pressure and OH* emission intensity spectrums under P_fM_a, P_aM_f and P_fM_f cases.

3.2 Flame CH* Distribution

To visualize the flame structures, temporal CH* images under P_fM_a, P_aM_f, and P_fM_f conditions are acquired to investigate instantaneous characteristics in this part. From the OH* oscillation frequency shown in Figure 3, it can be calculated that the flame oscillation period of P_aM_f and P_fM_f conditions is about 8 ms. The succession of eight instantaneous CH* images under P_fM_a, P_aM_f, and P_fM_f conditions are displayed in Fig. 4. For the P_fM_a case, the CH* image is a compact detachment V-shaped flame, and its root is located at the pilot nozzle outlet. Meanwhile, periodic fluctuation of intensity and distribution is not reported from the successive CH* images. For the P_aM_f case, the CH* image is a bowl-shaped flame structure. A greatly wrinkled area and local high-intensity CH* region exist on the flame surface due to the high levels of turbulent swirling flow. The flame also shows periodic fluctuation in the chamber, which indicates that the flame has become unstable. Because the heat load increases to 34.7 kW in the P_fM_f case, CH* intensity gets significantly higher than that in the P_fM_a and P_aM_f cases. The interaction between the pilot and main flames causes the more drastic expansion of the main flame along the radial direction and the more intense oscillation of the pilot flame.
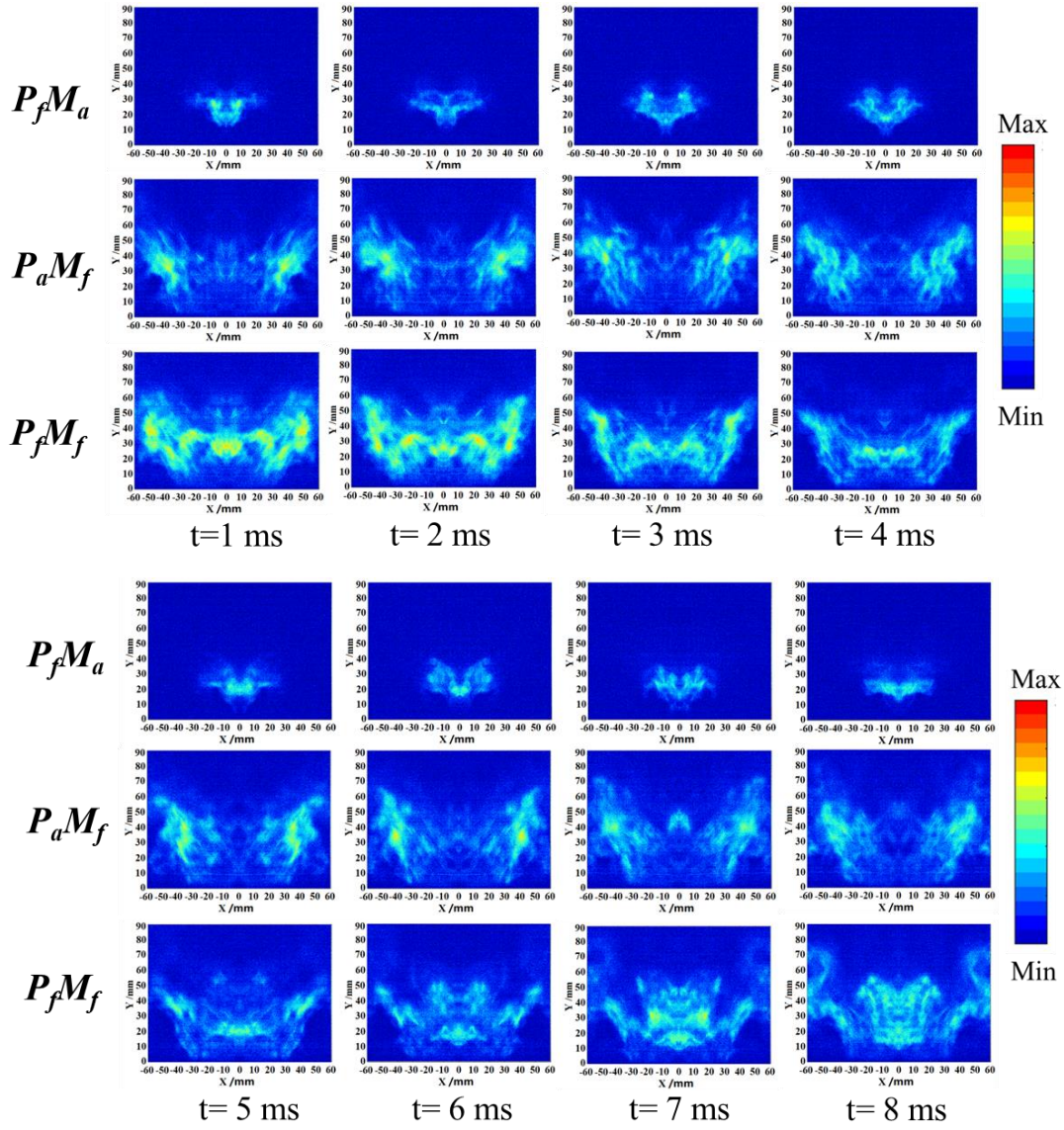
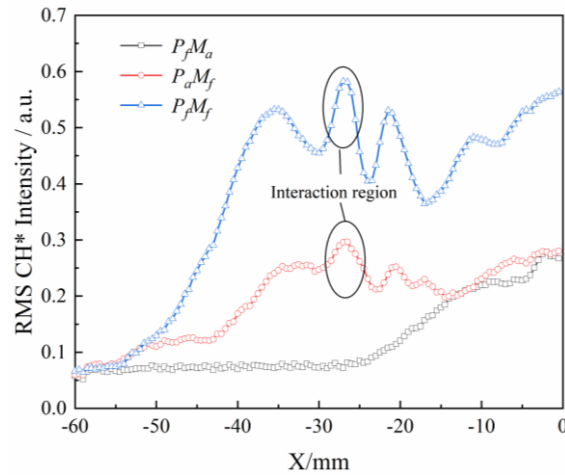**Figure 4. Temporal CH* images within 8 ms under P_fM_a, P_aM_f and P_fM_f cases.**

Figure 5. RMS CH* intensity profiles under P_fM_a, P_aM_f and P_fM_f cases.

RMS CH* intensity profiles of the divided parts along radial direction under P_fM_a, P_aM_f, and P_fM_f conditions are shown in Fig. 5 to reveal the location of high levels of flame oscillation. For the P_fM_f case, the peak location of RMS CH* intensity is near the flame interaction region, which means the flame oscillates strongest in this region. Compared with the P_aM_f case, the RMS CH* intensity profile shows one more peak on the left side of the flame interaction zone, which corresponds to the outer shear layer of the main stage swirling flow. To illustrate why the peak exists near this region, the successive vorticity maps of the P_fM_f case are presented in Fig. 7, which suggest that a vortex with a high vorticity level is induced at the outer shear layer of main stage swirling flow, and this may account for the intense instability of flame surface.

3.3 Time-averaged velocity fields

The analysis of the time-averaged velocity field is performed by applying high-speed PIV under reacting and non-reacting conditions. For the P_aM_a case, the streamlines superimposed with the axial velocity map indicate the pilot swirling flow interacts with the main swirling flow and they merge together to form a main recirculation zone RZ1.

For the P_fM_a case, results suggest that the pilot swirling flow turns to the main swirling flow and they merge together to impinge on the chamber wall. It is also obvious to find two recirculation zones named RZ1 and RZ2 in Fig. 6, and they are distributed respectively at the pilot swirler exit plane and inner shear layer. The gas density of the pilot swirling flow dramatically decreases due to combustion, which may account for the formation of recirculation zone RZ1.

The gas density decreases more intensely due to the increase of heat load under P_aM_f and P_fM_f cases, which leads to the increase of velocity magnitude at the swirler exit plane. For the P_aM_f case, the density of the main swirling flow decreases after combustion, and the expansive flow exerts a radial force on the pilot swirling flow so that the pilot swirling flow develops vertically to downstream. Fig. 6 shows the main recirculation zone is destroyed by the pilot swirling flow in this case, which probably leads to the main stage flame oscillation and thermo-acoustic instability.

For the P_fM_f case, the hot gas of the pilot stage expands and suppresses the radial force from the main swirling flow, so that the pilot swirling flow turns to the main swirling flow and both swirling jets remerge together. Fig. 6 shows the main recirculation zone is restored in this case, which helps roll back the burned gas to stabilize the pilot and main flames. The dynamic pressure spectrum shown in Fig. 3 also indicates that the amplitude decreases by approximately 76.8% compared with the P_aM_f case.
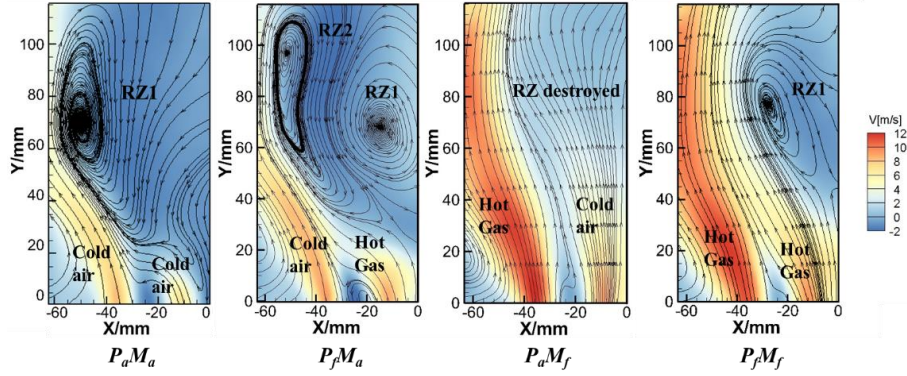
Figure 6. Time-averaged flow fields under P_aM_a, P_fM_a, P_aM_f and P_fM_f cases.

The time-averaged flow field structures under different operating conditions show that the main and pilot swirling flow interact with each other along the main swirling flow inner shear layer. However, different interaction behaviors and mechanisms make the flow field structures complex and changeable at the burner exit plane. When the main stage is only provided with air, no matter what condition the pilot stage is operated, such as P_aM_a and P_fM_a cases, the typical recirculation zone is always observed at the swirler exit plane. When the main stage is operated with a swirling flame, the pilot stage operating conditions play a vital role in the flow field structures. The typical recirculation zone disappears while the pilot stage is only provided with air, on the contrary, the typical recirculation zone restores while the pilot stage is also operated with swirling flame.

3.4 Instantaneous velocity fields dynamic characteristics

It can be seen from the time-averaged flow fields that the swirling flame has an important influence on the formation and distribution characteristics of the vortex. Fig. 7 shows the procedure of vortex shedding and vorticity distribution of the transient flow fields within 6 ms under different conditions.
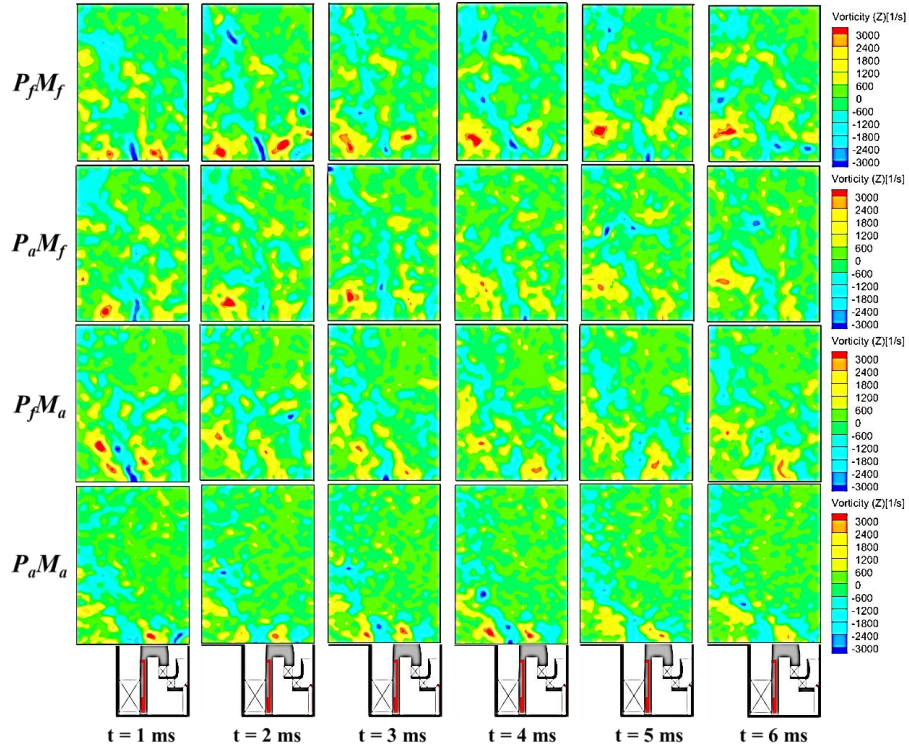
Figure 7. Temporal vorticity maps within 6 ms under P_aM_a, P_fM_a, P_aM_f and P_fM_f cases.

For the non-reacting P_aM_a condition, small vortices with low vorticity intensity are generated in the shear layer of the swirling flow, and the strength of the vorticity is damped while traveling downstream. Under the P_fM_a condition, the orderly large-scale vortex structure is not induced in the flow field due to stable combustion and low heat load. Only a series of small vortices are generated at the swirler outlet due to the flow instability of the shear layer. The vorticity intensity is similar to that under P_aM_a condition, and the vortex also dissipates rapidly while traveling downstream.

With the increase of heat load, large-scale vortex structures are induced at the swirler outlet under both P_aM_f and P_fM_f conditions, and the vortex intensity of the P_fM_f condition is obviously higher than that of the P_aM_f condition. For P_aM_f condition, affected by the main swirling flame, a large-scale vortex is only induced at the shear layer of the main swirling flow. However, since the pilot stage is only provided with air, the large-scale vortex is still uninduced near the shear layer of the pilot swirling flow. For the P_fM_f condition, affected by the pilot and main swirling flames, large-scale vortex structures can be detected at both the pilot and main swirling flow shear layers. Given the influence of combustion and flame, to some extent, the intensity of large-scale vortex under reacting cases can be considered as proportional to the combustion heat load.

The POD method is used to analyze the dynamic characteristics of the large-scale vortex in the flow field. Fig. 8 shows the first 10 modes of energy fraction profiles of the flow field POD decomposition under different testing conditions. The mode energy fraction characterizes the contribution rate of each mode to the dynamic characteristics of the instantaneous temporal flow fields. The larger the value of a certain mode energy fraction, the greater the impact on flow field dynamic characteristics, so it can be used to characterize the

11

most significant features in the flow field. Results indicate that the mode energy fractions of the P_aM_a and P_fM_a conditions are much lower than the P_aM_f and P_fM_f conditions. However, although the first two modes energy fraction of P_aM_f and P_fM_f condition is pretty higher, the mode energy fraction damps rapidly. The first mode energy fractions of the flow field under the P_aM_a, P_fM_a, P_aM_f, and P_fM_f conditions are 4.3 %, 6 %, 9.7 %, and 16.2 %, respectively. The trend of the first mode energy fraction under different testing conditions also shows that the increase of combustion heat load enhances the strength of large-scale vortices in the flow field.
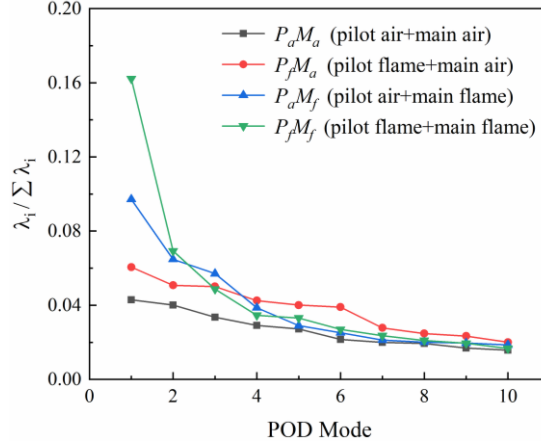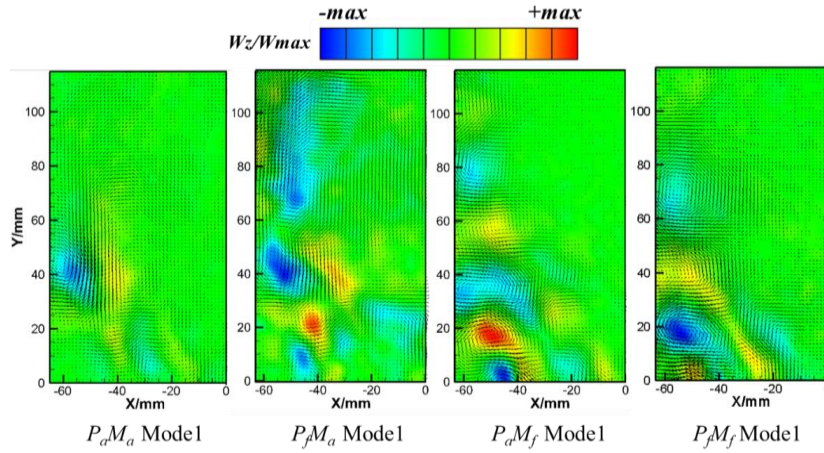

Figure 8. Flow field POD mode energy fractions under P_aM_a, P_fM_a, P_aM_f and P_fM_f cases.

Fig. 9 shows the vorticity maps superimposed with velocity vectors of the POD mode 1 under different testing conditions. For the P_aM_a, condition, only a few vortices are extracted near the outer shear layer of the main swirling flow, and the vorticity intensity of the vortices is low. For the P_fM_a condition, more vortices are induced in the flow field, and the vorticity intensity gets higher. However, the vortices are still irregularly distributed downstream of the swirler outlet. For the P_aM_f and P_fM_f cases, regular and periodic vortices appear in the outer shear layer of the main swirling flow, and the energy gradually damps as it moves downstream. The energy dissipation of the vortex in the P_fM_f case is faster than that in the P_aM_f case due to the flame interaction between the main and pilot stages. The results mentioned above reveal that the increase of combustion heat load leads to the accelerated expansion of gas, which induces higher intensity vortices in the swirling flow shear layer, while the flame interaction between the pilot and main stage accelerates the energy dissipation of vortices.

To analyze the dynamic characteristic of the large-scale vortex, the time coefficient value of the POD first mode is used to extract the vortex shedding frequency by fast Fourier transform (FFT) under different testing conditions. The spectrums shown in Fig. 10 indicate that the FFT results of the first mode time coefficient value mode have no oscillation frequency under P_aM_a and P_fM_a cases, and this also suggests that periodic large-scale vortex is not induced in the flow field. The dominant frequency of the time coefficient spectrum in the P_aM_f case is 115 Hz, indicating that the frequency of shedding vortex generated by the swirling flow shear layer of the main stage is 115 Hz, which is locked with the frequency of thermo-acoustic instability mode under this condition. However, the time coefficient spectrum

in the P_fM_f case has the dominant frequencies of 68 Hz and 109 Hz, which indicates that the frequency of large-scale shedding vortex in the flow field is not only different from the vortex shedding frequency of the P_aM_f condition but also not locked with the thermo-acoustic instability frequency of the P_fM_f case. The results of the P_aM_f case show that acoustic-velocity-flame instabilities are coupled mutually under the single swirling flame self-excited oscillation condition. However, for the P_fM_f case, because the pilot flame interacts with the main flame, the flow instability frequency induced by flame and pressure oscillations changes significantly, and the coupling between acoustic-velocity-flame instabilities is also destroyed.

Figure 9. Vorticity maps superimposed with velocity vectors of POD mode 1 under P_aM_a, P_fM_a, P_aM_f and P_fM_f cases.
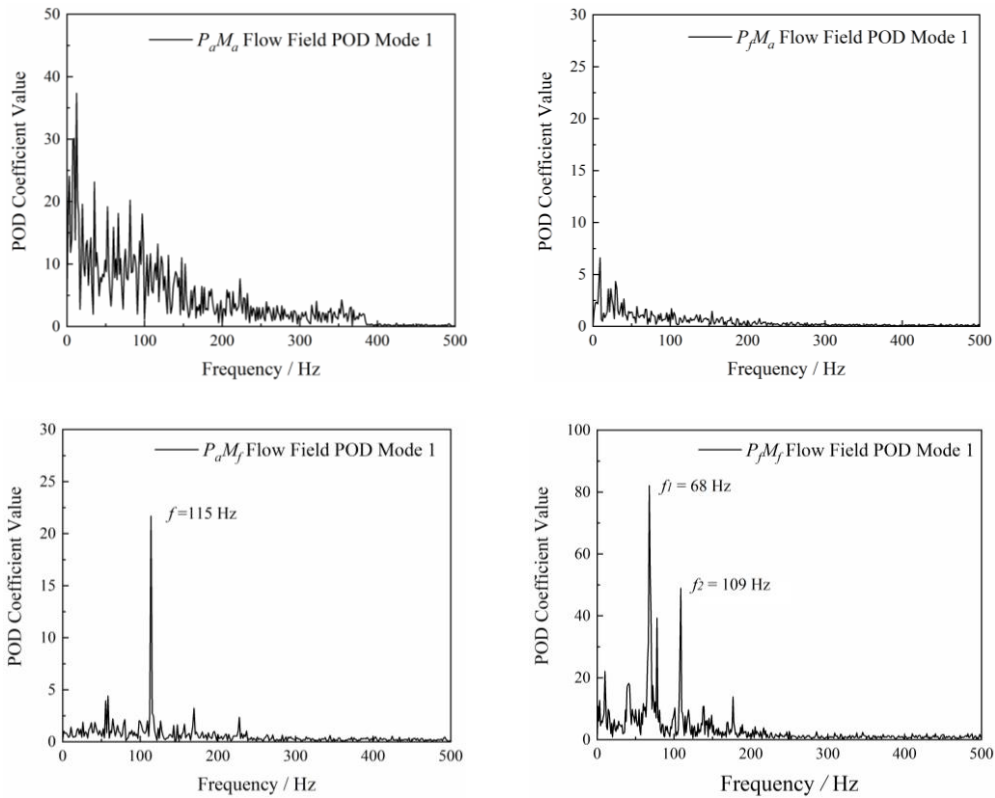

Figure 10. Time coefficient value spectrums of POD mode 1 under different cases.

3.5 Combustor acoustic mode analysis

From the results of flow dynamics and combustion instability, it can be summarized that the couple of acoustic-velocity-flame plays an important role in combustion instability. In order to understand the flow-flame-acoustic interaction, the simplified acoustic mode analysis is conducted. To some extent, longitudinal acoustic modes are thought to be significantly important in flow-flame-acoustic interaction [31]. In this work, the acoustic modes analysis is conducted based on the open-source low-order simulator OSCILOS-LONG [32].

As shown in Fig. 1, The test rig includes a plenum and a flame tube. The inlet of the plenum and outlet of the flame tube are represented by the blue and green lines in Fig. 11, respectively. The inlet boundary is considered as a rigid wall. The outlet of the flame tube is open to the atmosphere. For simplicity, the heat resource is considered as a compact flame indicated by the red line. The flame is stabilized at the plenum outlet. The plenum is a cylindrical tube with a length of 270 mm and a diameter of 87 mm. The length and hydraulic diameter of the flame tube exhaust pipe are 1230 mm and 140 mm, respectively.
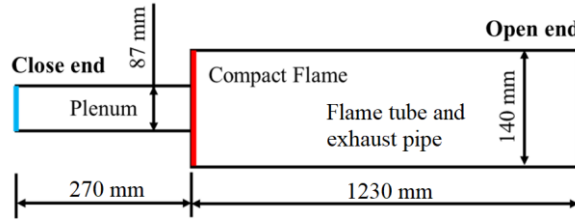
Figure 11. Low-Order combustor acoustic mode simulator.

The mean velocity at the inlet of the plenum is U_0=10.1 m/s. The mean pressure is P_0=1 bar and the mean temperature is T_0=300 K. Methane is used as the fuel and the global equivalence ratio is φ= 0.67. The combustion efficiency η is set to 0.97. Hence, it is capable of calculating the mean thermal physical properties in different sections. The linear flame transfer function n-tau model is applied to define the unsteady heat source based on the experimental results [33]. The flame transfer function (FTF) gain profiles of P_aM_f and P_fM_f cases are shown in Fig. 12. Both cases show strong forced response characteristics in the disturbance range of 100 to 200 Hz. However, the delay time is different. The delay time of the P_aM_f case is about 16.2 ms, and that of the P_fM_f case is approximately 11.1 ms.
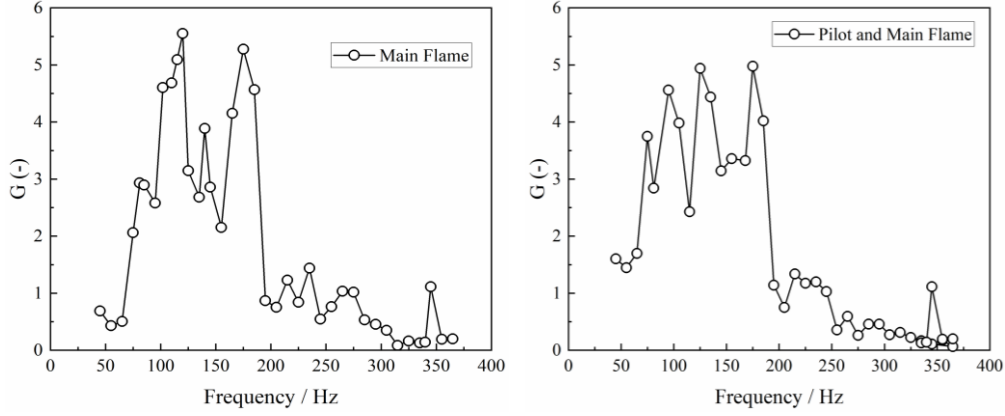
a) P_aM_f FTF Gains profile   b) P_fM_f FTF Gains profile

Figure 12. FTF gains profiles under P_aM_f and P_fM_f cases.

In order to analyze the stability of the system in the frequency domain. the time domain function is transformed into the complex frequency domain by Laplace transform. As shown in Fig. 13, the real part and the imaginary part are taken as the horizontal and vertical axes respectively to show the change of the characteristic frequency and growth rate of the acoustic mode of the system. The main acoustic modes of the system under P_aM_f and P_fM_f conditions are represented by a blue pentagon and red pentagram. When the growth rate is negative, it indicates that the system will not trigger thermo-acoustic instability mode at this frequency. When the growth rate is positive, it indicates that the acoustic energy in the system will continue to increase and may become a potential instability mode.

The results of Fig. 13 show that in the frequency range of 0 to 500 Hz, there are several potential unstable modes in the combustion system under the P_aM_f condition, and the growth rate is higher than that under the P_fM_f condition. The characteristic frequency $f_1 = 117$ Hz, the growth rate is 79.72 rad/s, and this characteristic acoustic mode frequency of the combustion chamber is basically consistent with the thermo-acoustic instability frequency. On the contrary, there are only two potentially unstable acoustic modes in the combustion system under P_fM_f condition, and the growth rate is significantly reduced. The growth rate of characteristic acoustic mode frequency $f_1 = 123$Hz is 67 rad/s. This acoustic mode frequency of the combustion system is also basically consistent with the thermo-acoustic instability frequency. The interaction between the pilot flame and the main flame has a significant effect on the characteristic acoustic mode frequency and growth rate of the combustion chamber, resulting in different thermo-acoustic instability characteristics under P_aM_f and P_fM_f conditions.

a) Characteristic modes for P_aM_f case   b) Characteristic modes for P_fM_f case
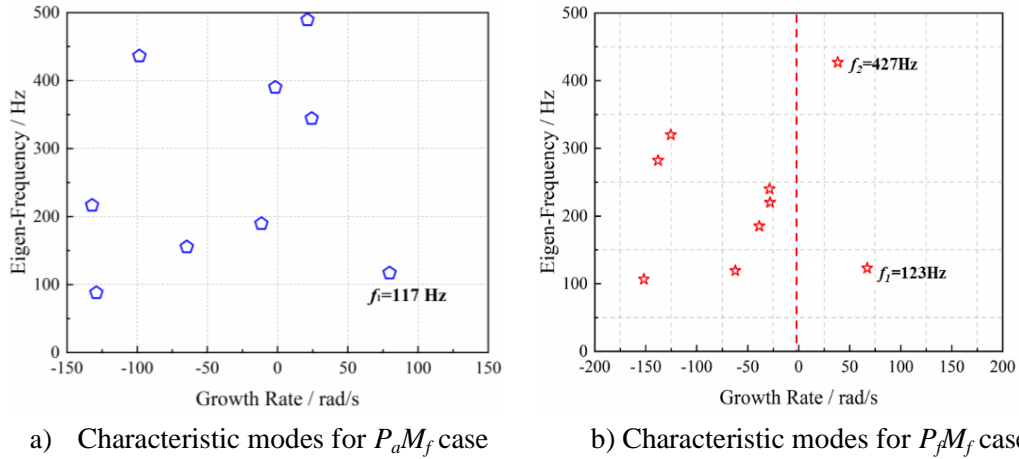
Figure 13. Simplified combustor acoustic mode results for P_aM_f and P_fM_f cases.

4. Conclusions

Under the condition of ambient temperature and pressure, the flow and thermo-acoustic instability of the stratified burner were detailed studied by means of high-frequency PIV, high-speed camera, photomultiplier tube, and dynamic pressure sensors. Combined with the simplified acoustic mode calculation of the combustion chamber, the influence of the main stage flame and the stratified flame on the acoustic modes of the combustion chamber was obtained. The conclusions are as follows:

For the P_fM_a case, the combustion is stable. For the P_aM_f case, the main peak values of dynamic pressure and heat release are both visible at a frequency of 115 Hz, and the peak value of pressure is 2947 Pa. For the P_fM_f case, the dominant frequency of pressure and heat release is slightly shifted, and it is increased by 5 Hz. However, the peak value of pressure is 683 Pa. The pilot stage flame reduces the pressure peak value of the main stage flame by 76.8 %, which effectively suppresses the thermo-acoustic instability in the P_aM_f case. The interaction between the pilot stage flame and the main stage flame has a significant effect on the characteristic acoustic mode frequency and growth rate of the combustion chamber. Compared with the P_aM_f case, the potential unstable acoustic modes of the P_fM_f case are suppressed, and the growth rate of the unstable acoustic mode also decreases significantly.

When the main stage is operated with swirling air, whether the pilot stage is operated with swirling air or swirling flame, the stable main recirculation zone always can be observed at the burner exit. However, when the main stage is operated with a swirling flame, the swirling air from the pilot stage will destroy the main recirculation zone, which is detrimental to the combustion stability of the main stage swirling flame. When the pilot stage is converted into a swirling flame, the main recirculation zone re-appears. The increase in heat load leads to the accelerated expansion of the gas, which induces a stronger vortex in the swirling flow shear layer. The interaction between the pilot flame and the main flame accelerates the dissipation of the vortex. Especially, For the P_aM_f case, the acoustic-velocity-flame instability frequency can be locked. However, For the P_fM_f case where the pilot and the main flames interact with each other, the frequency of the vortex shedding induced in the flow field is different from the thermo-acoustic instability frequency.

Compared with the P_fM_a and P_aM_f cases, the main stage and pilot stage flames interact with each other in the P_fM_f case, resulting in an increase in the flame angle of the main stage. The heat release fluctuation at the flame interaction region is the most intense, and the large-scale vortex in the outer shear layer of the main stage also causes the flame to produce severe oscillation.

Based on the results obtained, the interaction between the pilot stage flame and the main stage flame has a significant effect on the flow-thermal-acoustic characteristics. To better understand the interaction mechanism of the stratified flame, The future directions of research and development of the topic can be considered for two parts. One is the effects of equivalence ratio distribution between pilot stage flame and the main stage flame on the flow-thermal-acoustic characteristics. The other is the effects of swirl intensity arrangements between pilot stage and the main stage on the flow-thermal-acoustic characteristics.

Acknowledgments

References

[1] Han X, et al. Flame interactions in a stratified swirl burner: flame stabilization, combustion instabilities and beating oscillation [J]. Combustion and Flame, 2020, 212: 500-509.

[2] Mongia H C, et al. Challenges and progress in controlling dynamics in gas turbine combustors [J]. Journal of Engineering for Gas Turbines and Power, 2003, 19: 822-829.

[3] Zhang C, et al. Experimental investigations on central vortex core in swirl spray flames using high-speed laser diagnostics[J]. Physics of Fluids, 2023, 35: 035130.

[4] Yan B, et al. Simultaneous visualization of instantaneous unburnt and preheating zones in turbulent premixed flames under transverse acoustic excitations[J]. Physics of Fluids, 2022, 34: 095107.

[5] Zhang B, et al. Contributions of hydrodynamic features of a swirling flow to thermoacoustic instabilities in a lean premixed swirl stabilized combustor[J]. Physics of Fluids, 2019, 31: 075106.

[6] Wang G F, et al. Flame propagation patterns and local flame features of an annular combustor with multiple centrally staged swirling burners[J]. Physics of Fluids, 2023, 35: 085134.

[7] Menon S. Acoustic-vortex-flame interactions in gas turbines [J]. Progress in Astronautics and Aeronautics, 2005, 210: 277.

[8] Balachandran R, et al. Experimental investigation of the nonlinear response of turbulent premixed flames to imposed inlet velocity oscillations [J]. Combustion and Flame, 2005, 143(1-2): 37-55.

[9] Bellows B D, et al. Flame transfer function saturation mechanisms in a swirl-stabilized combustor [J]. Proceedings of the Combustion Institute, 2007, 31(2): 3181-3188.

[10] Santosh H, et al. Premixed flame response to equivalence ratio perturbations [J]. Combustion Theory and Modelling, 2010, 14(5): 681-714.

[11] Bellows B D, et al. Nonlinear flame transfer function characteristics in a swirl-stabilized Combustor [J]. Journal of Engineering for Gas Turbines and Power, 2007, 129(4): 954-961.

[12] Thumuluru S K, et al. Characterization of acoustically forced swirl flame dynamics [J]. Proceedings of the Combustion Institute, 2009, 32(2): 2893-2900.

[13] Schimek S, et al. An experimental investigation of the nonlinear response of an atmospheric swirl-stabilized premixed flame [J]. Journal of Engineering for Gas Turbines and Power, 2011, 133(10): 101502.

[14] Schimek S, et al. Amplitude-dependent flow field and flame response to axial and tangential velocity fluctuations [J]. Journal of Engineering for Gas Turbines and Power, 2015, 137(8): 081501.

[15] Terhaar S, et al. Impact of shear flow instabilities on the magnitude and saturation of the flame response [J]. Journal of Engineering for Gas Turbines and Power, 2014, 136(7): 071502.

[16] Oberleithner K, et al. Shear flow instabilities in swirl-stabilized combustors and their impact on the amplitude dependent flame response: a linear stability analysis [J]. Combustion and Flame, 2015, 162(1): 86-99.

[17] Palies P, et al. Experimental study on the effect of swirler geometry and swirl number on flame describing functions [J]. Combustion Science and Technology, 2011, 183(7): 704-717.

[18] Palies P, et al. The combined dynamics of swirler and turbulent premixed swirling flames [J]. Combustion and Flame, 2010, 157(9): 1698-1717.

[19] Terhaar S, et al. Combustion and flame suppression and excitation of the precessing vortex core by acoustic velocity fluctuations: an experimental and analytical study [J]. Combustion and Flame, 2016, 172: 234-251.

[20] Ma J L, et al. Influence of the co- and counter-swirl on combustion instability of the centrally staged combustor[J]. Physics of Fluids, 2023, 35: 087127.

[21] Chong C T, et al. Effect of mixture flow stratification on premixed flame structure and emissions under counter-rotating swirl burner configuration [J]. Applied Thermal Engineering, 2016, 105: 905-912.

[22] Kim K T, et al. The nonlinear heat release response of stratified lean-premixed flames to acoustic velocity oscillations[J]. Combustion and Flame. 2011, 158: 2482-2499.

[23] Han X, et al. Flame macrostructures and thermoacoustic instabilities in stratified swirling flames [C] //Proceedings of the Combustion Institute, 2019, 37: 5377-5384.

[24] Lv G P, et al. Large eddy simulations of pilot-stage equivalence ratio effects on combustion instabilities in a coaxial staged model combustor[J]. Physics of Fluids, 2023, 35: 095134.

[25] Weber R, et al. Combustion accelerated swirling flows in high confinements. Prog. Energy Combust. Sci. 1992; 18 :349–67.

[26] Procacci A, et al. Multi-scale proper orthogonal decomposition analysis of instabilities in swirled and stratified flames[J]. Physics of Fluids, 2022, 34: 124103.

[27] Krasilnikov V A, et al. Atmospheric turbulence and radio-wave propagation [J]. Monograph on Radio-wave Propagation in the Troposphere, 1962, 62: 145.

[28] Sirovich L. Turbulence and the dynamics of coherent structures. I-coherent structures [J]. Quarterly of Applied Mathematics, 1987, 45(3): 561-571.

[29] Wyatt C, et al. The effect of variable fuel staging transients on self-excited instabilities in a multiple-nozzle combustor[J]. Combustion and Flame, 2018, 194: 472-484.

[30] Richards G A, et al. Characterization of oscillations during premix gas turbine combustion[J]. Journal of Engineering for Gas Turbines and Power, 1998, 120(2): 294-302.

[31] MENON S. Acoustic-vortex-flame interactions in gas tur-bines[J]. Progress in Astronautics and Aeronautics, 2005, 210: 277.

[32] Li J X, et al. Open-Source combus-tion instability low order simulator (OSCILOS–Long). Technical report, 2017.

[33] Liu W J, et al. Dynamic Response of Stratified Flames to Acoustic Excitation in a Multi-Swirler Model Combustor [C] //Proceedings of the ASME Turbo Expo 2022: Turbomachinery Technical Conference and Exposition. Volume 3B: Combustion, Fuels, and Emissions. Rotterdam, Netherlands. June 13–17, 2022. V03BT04A035. ASME.